This article appeared as:
P. Li and S. Biwa, The SH0 wave manipulation in graded stubbed plates and its application to wave focusing and frequency separation, *Smart Materials and Structures*, 28 (2019), 115004. DOI: 10.1088/1361-665X/ab3ef0

The SH0 wave manipulation in graded stubbed plates and its application to wave focusing and frequency separation

Peng Li[1, 2], Shiro Biwa[1]

[1] Department of Aeronautics and Astronautics, Graduate School of Engineering, Kyoto University, Katsura, Nishikyo-ku, Kyoto 615-8540, Japan

[2] Department of Civil Engineering, Xi'an Jiaotong University, Xi'an, Shaanxi 710049, China

Corresponding author, Peng Li, **E-mail:** jerrylee@xjtu.edu.cn

Abstract: In this study, a methodology to artificially control the propagation of fundamental shear horizontal (SH0) waves in elastic plates is proposed using stubs with spatially graded height, and two novel phenomena, wave focusing and low-pass wave filtering, are realized. As a basis for this, the band structure analysis is carried out for an aluminum plate with hexagonally arranged stubs, and the relationships between the wave velocity, the band gap and the stub height are established. Based on these results, omni-directional SH0 wave-based Luneburg and Maxwell fish-eye lenses, as well as low-pass wave filter, are designed artificially using multiple stubs with spatially graded heights. It is demonstrated that both of the lenses exhibit good focusing ability, with the focusing size smaller than the wavelength. Additionally, they can work with a finite bandwidth around the design frequency. It has also been revealed both in time and frequency domain simulations that the SH0 wave with a lower frequency can travel over a longer distance when it enters the low-pass wave filter, which demonstrates its frequency separation capability.

Keywords: shear horizontal waves, refractive index, Luneburg lens, Maxwell fish-eye lens, low-pass wave filter.

1 *Introduction*

While the Lamb wave-based nondestructive evaluation (NDE) and structural health monitoring (SHM) techniques are applied extensively for plate-type structures [1, 2], the shear horizontal (SH) plate wave-based techniques have unique appealing features and potential advantages [3-5]. Since the SH plate waves have no out-of-plane particle displacement, the wave propagation will be less affected by the presence of surrounding liquid media [3]. Furthermore, the fundamental mode of SH plate waves (SH0 wave) is non-dispersive, i.e., the phase and group velocities are determined by the material parameters and do not depend on the frequency or the plate thickness. This frequency-independent feature offers certain convenience and flexibility in NDE/SHM applications. Since the SH0 wave packet will not be broadened as the propagation distance increases, the signal from defects can be easily recognized thus reducing complexity of signal processing [4]. It has also been demonstrated experimentally that the nonlinear third-harmonic of SH0 wave is more sensitive to the microstructural change of materials as a precursor of early-stage damage than the second-harmonics of Lamb waves [5].

SH plate waves also find applications in surface acoustic wave (SAW) devices for chemical and biochemical sensing, which mainly consist of a thin surface layer supported on a substrate [6-8]. These devices use the perturbations of wave properties such as velocity, phase and amplitude caused by the surrounding media to characterize their physical and chemical properties [9-11]. Because of the in-plane nature of their motion, the SH plate waves have their energy essentially confined in the surface layer without energy leakage into the surrounding inviscid liquid media and thus can travel a long distance, which makes the SH plate wave-based SAW devices particularly suitable for liquid-phase sensing.

For both NDE/SHM and acoustic device applications, the generation of SH waves in plates has been investigated experimentally by a number of investigators [2, 12-15]. Ideally, it is also important to achieve the desired SH wave field, or even control the wave propagation behavior, in plates for even broader applications. Recently, novel properties of phononic crystals (PCs) and metamaterials are attracting increasing attention regarding their capability to manipulate the propagation of acoustic waves [16-24]. Since SH waves are governed by the same partial differential equations as acoustic waves in fluids, the methodology of changing the acoustic wave propagation properties using PCs and metamaterials can be directly utilized to control SH waves as already reported regarding, among others, the band gap (BG) properties by periodic microstructures [25-28], cloaking [29-30], rainbow trapping [31], metasurfaces [32] and collimation [33]. In these works [25-33], the theoretical problems were formulated in two dimensions, which was natural considering the original definition of SH waves. On the other hand, finite sources in a plate cannot create pure SH waves but accompany other displacement components. Furthermore, they undergo amplitude decay due to wave diffraction. Therefore, to examine the control of SH wave propagation from finite sources, a three-dimensional analysis is necessary.

In this paper, a method to control the propagation of SH0 waves in elastic plates is examined based on the three-dimensional numerical analysis. In particular, the focusing as well as frequency separation of SH0 waves is demonstrated by arranging circular cylindrical

stubs with spatially graded heights on the plate. To examine the possibility of SH0 wave control, the pertinent dispersion relation of a thin plate with hexagonally arranged stubs is first considered. Utilizing the property of the horizontal shear-dominated wave in this structure that its velocity changes monotonically with the stub height, the SH0-wave-based Luneburg and Maxwell fish-eye lenses are designed, followed by a comprehensive FEM validation process in both time and frequency domains. Furthermore, the design scheme of a low-pass filter is discussed based on the stub-height dependence of the band gap, and its frequency separation capability is demonstrated by a specific example.

2 *The band structure of SH0 waves*

As a basis to design the omnidirectional SH0 wave-based lens and low-pass wave filter, the band structure of elastic waves in a periodically stubbed plate is first examined. Circular cylindrical stubs are distributed in the hexagonal array with the lattice constant a on a flat elastic plate lying in the x-y plane. A unit cell, consisting of the stub with its diameter $2b$ attached on the surface of the plate, is adopted as shown in Fig. 1(a). The plate thickness is denoted by h and the stub height is h'. It is assumed that the plate and the stubs are made of the same isotropic elastic solid. In this paper, stubbed plates made of aluminum (density ρ = 2700 kg/m^3, Lamé's constants λ = 51.1 GPa and μ = 26.3 GPa) consisting of the unit cells with the lattice constant a = 10 mm, the plate thickness $h = 0.5a$, the stub radius $b = 0.3a$ and the variable stub height h' are considered. The first Brillouin zone is selected as Fig. 1(b). Because of the periodicity, the Floquet boundary conditions are applied on the six lateral sides of the hexagonal plate, and the other surfaces are set as traction free. For the wave vector varying along the edge of the first Brillouin zone, the corresponding frequencies can be obtained by solving the eigenvalue problem. The numerical analyses presented in this paper are all performed with the help of Comsol Multiphysics software by using tetrahedral elements to discretize the structure. For the band structure calculation, the element size is typically chosen as 1 mm, i.e., one tenth of the lattice constant a. The eigenvector corresponding to the specific eigenfrequency represents the modal displacement field.

In a flat homogeneous elastic plate, the displacement components of pure SH waves can be represented by [25, 28, 31]

$$u_x = u_z = 0\,,\quad u_y = u(x,z,t)\,, \tag{1}$$

which obey the governing equation

$$\mu\left(\frac{\partial^2 u_y}{\partial x^2}+\frac{\partial^2 u_y}{\partial z^2}\right)=\rho\frac{\partial^2 u_y}{\partial t^2}\,. \tag{2}$$

The velocity of the non-dispersive SH0 wave is given by $c_{\mathrm{SH0}}=\sqrt{\mu/\rho}=3121\,\mathrm{m/s}$ for aluminum. In the presence of stubs, however, the motion in the plate is not purely shear horizontal but accompanied by the three-dimensional displacement field. Therefore, the band structure analysis is carried out within the three-dimensional framework, where all frequency branches obtained are associated with the three displacement components. In this situation,

however, it is possible to identify a branch for which the displacement mode is dominated by the shear horizontal component which is nearly uniform over the plate thickness. Therefore, the terminology of SH0 wave is also used in this paper to refer to such waves in the stubbed plate.

Fig. 1(c) shows the so-determined band structure of SH0 wave in the stubbed aluminum plate along the ΓM direction for different stub heights. The curve for $h' = 0$ in Fig. 1(c) originates at the Γ point and extends linearly, which indicates the non-dispersive property of SH0 wave in a homogeneous plate. With increasing stub height h', the dispersion becomes more and more evident and the slope of the curve decreases at low frequencies, which leads to reduced wave velocity. Additionally, some band gaps (BGs) emerge, exemplified by two BGs below 180 kHz when $h' = 0.4a$. In order to clearly demonstrate the BG features by the periodic stubs, the SH0 wave transmission through a finite system consisting of ten unit cells, connected to flat plates of thickness h as shown in Fig. 1(d), is also analyzed and the transmission spectrum is calculated as $T = 20\log_{10}\left(\left|u_y^{\text{out}}\right|_{\text{ave}} / \left|u_y^{\text{in}}\right|_{\text{ave}}\right)$, where $\left|u_y^{\text{in}}\right|_{\text{ave}}$ and $\left|u_y^{\text{out}}\right|_{\text{ave}}$ are respectively the displacement amplitudes of the incident and transmitted SH0 waves averaged over the exciting and the receiving cross-sections. Two perfectly matched layers (PMLs) are employed at both ends to prevent unnecessary wave reflections. The maximum element size is set to be 1.25 mm for this analysis. By varying the excitation frequency of the incident SH0 wave, the transmission spectra are calculated as shown in Fig. 1(c). When the excitation frequency is located in the BGs, the SH0 wave propagation in the x direction is prohibited, which qualitatively validates the results of the band structure analysis. Moreover, the dispersion curve becomes almost flat near the edge of the first Brillouin zone, i.e., the M point, which means that the group velocity of the SH0 waves is reduced and approaches zero. The mode shape at the M point represented by u_y, illustrated in Fig. 1(e) when $h' = 0.6a$, shows that the stub vibrates significantly with the substrate plate being almost motionless, and hence most of the vibration energy is trapped in the stub. With increasing stub height, the central frequency of the first BG decreases. The Equi-Frequency Contours (EFCs) of the periodic structure are shown in Fig. 1(f) when $h' = 0.4a$. The center of the hexagon stands for Γ point, and any vector emitting from Γ represents the wave propagation direction. Since the EFCs below 84 kHz are nearly circles, it is expected that the stubbed plate exhibits good isotropy and the group velocity coincides with the normal direction to the EFC and points towards the frequency increment.

Based on the above findings, the artificial manipulation of SH0 waves is considered in this paper with the aid of appropriate spatial grading of the stub height. In what follows, two kinds of phenomena, i.e., wave focusing and frequency separation, will be realized via different configurations of graded stubs.

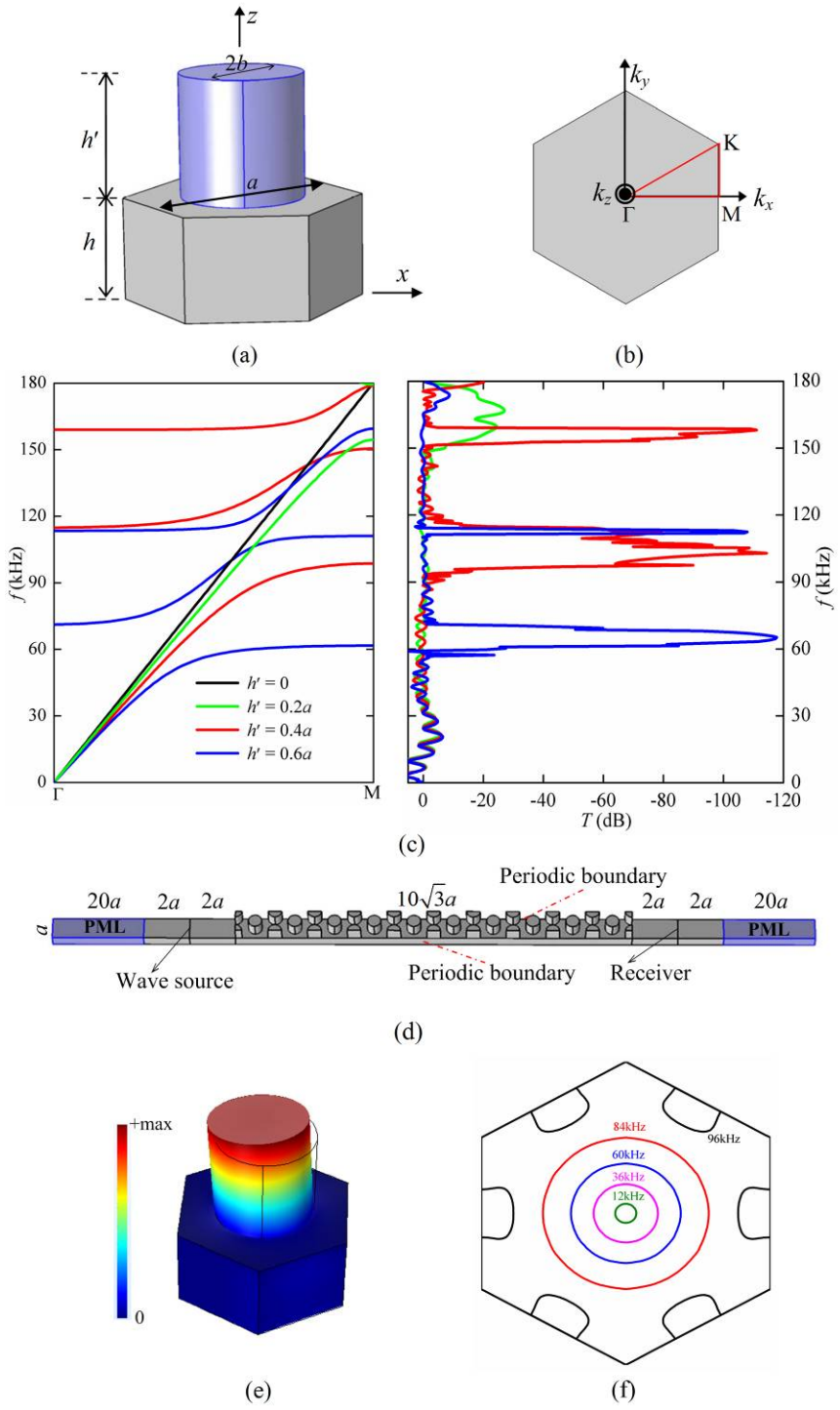

Figure 1 (a) the hexagonal unit cell with an attached stub; (b) the first Brillouin zone; (c) the band structures of SH0 wave for various stub heights and the transmission spectra; (d) the finite structure containing ten unit cells used for calculating the transmitted wave in the x direction; (e) the mode shape expressed by u_y at the M point when $h' = 0.6a$; (f) the equi-frequency contour when $h' = 0.4a$.

3 *The omni-directional SH0 wave-based Luneburg and Maxwell fish-eye lenses*

In this Section, two kinds of omni-directional SH0 wave-based lenses, i.e., Luneburg lens and Maxwell fish-eye lens, are designed to realize the wave focusing. The Luneburg lens and Maxwell fish-eye lens are respectively utilized to focus the plane wave and the wave from a point source. They require the refractive index profile $n(r)$ changing in the form of [34-36]

$$n(r) = \frac{c_0}{c} = \sqrt{2 - \left(r / R\right)^2} \text{ , for Luneburg lenses} \tag{3a}$$

$$n(r) = \frac{c_0}{c} = \frac{2}{1 + \left(r / R\right)^2} \text{ , for Maxwell fish-eye lenses} \tag{3b}$$

Here, r represents the radial coordinate and R is the lens radius. The wave velocities in the lenses and the surrounding medium are denoted by c and c_0, respectively. If a lens is designed properly with its refractive index according to Eq. (3a), the incident plane wave will focus at the opposite border of the lens, which is the feature of Luneburg lens. For Maxwell fish-eye lens, the wave from a point at the lens edge is focused at the opposite edge point when the refractive index varies according to Eq. (3b). Construction of the Luneburg and Maxwell fish-eye lenses using metamaterials has been already reported for acoustic waves [35, 38] and elastic waves in plates [36-37, 39]. In particular, Jin et al. [37] constructed these lenses for three guided waves in plates, including the SH0 mode, by using multiple inclusions with interior holes with graded radii. In this paper, the SH0 wave-based Luneburg and Maxwell fish-eye lenses are constructed by using multiple stubs with graded heights.

For SH0 waves, the refractive index can be calculated as $n(r) = c_{SH0}/c(r)$ [34, 37], in which $c(r)$ is the SH0 wave phase velocity in the lens and c_{SH0} is the SH0 wave velocity in the homogenous plate outside the lens. For the two SH0 wave-based lenses, the variations of refractive indices are shown in Fig. 2(a). Generally speaking, it is difficult to design a perfect lens which can exactly satisfy the refractive index variation pattern. In this study, inspired by Fig. 1(c), the Luneburg and Maxwell fish-eye lenses are realized approximately by distributed stubs with graded heights. With increasing stub height, the SH0 wave slows down gradually. Stubs with different heights delay the SH0 wave in different levels, and change the wave speed and refraction index gradually. This gives the basis for the present design scheme. When the wave frequency is assumed as f_0 = 40 kHz, the stub height corresponding to the desired phase velocity is given by the band structure analysis in Section 2. Using this relation, the stub height profile giving the desired spatial variation of the phase velocity (or refractive index) can be obtained as shown in Fig. 2(a). Based on this idea, the lens with diameter 0.2 m is constructed by arranging the hexagonal aluminum cells analyzed in Section 2 with graded stub heights. The lens is connected to a flat aluminum plate of the same thickness as the plate of the cell. The resulting stub arrangement for the Luneburg lens is shown in Fig. 2(b), which contains 373 cells. For the Maxwell fish-eye lens, the stub arrangement is the same as Fig. 2(b), except for the height values. Note that h' is greatest at the center of the lens and decreases gradually to zero towards the lens boundary, which is effective to reduce the wave reflection when an SH0 wave travels across the lens.

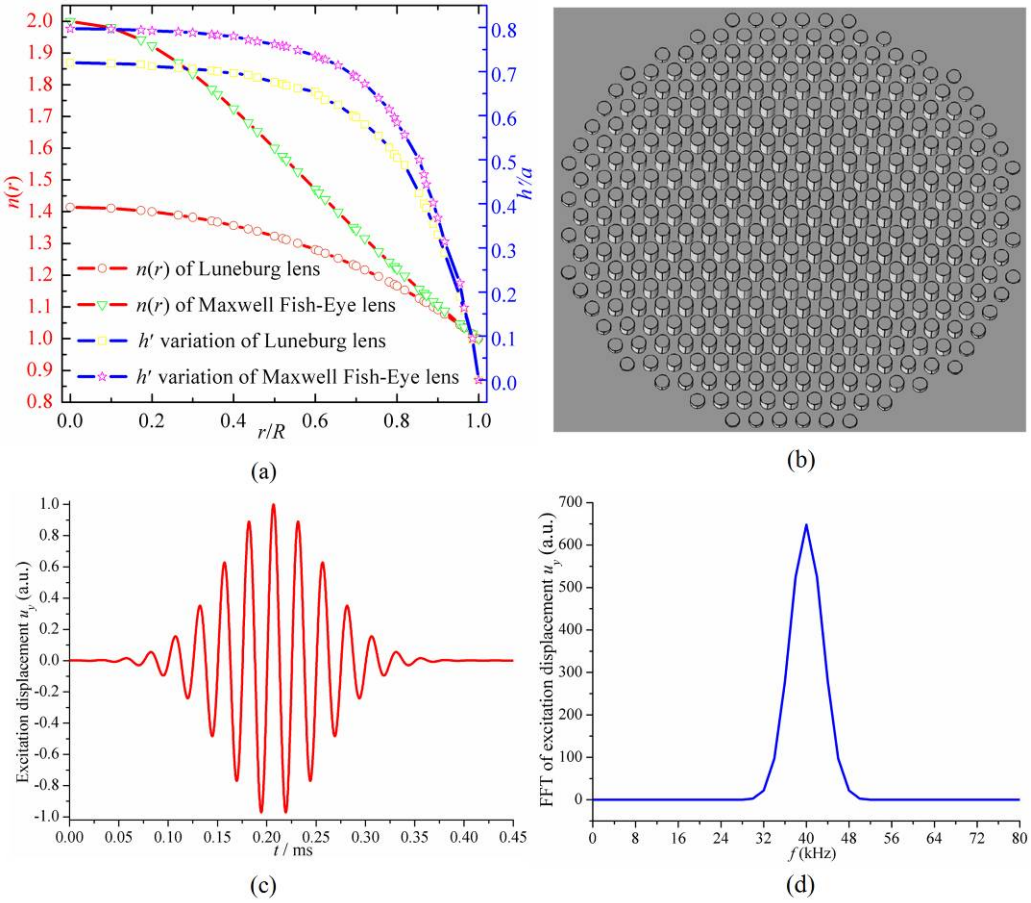

Figure 2 (a) the refractive index profiles $n(r)$ and the corresponding stub height variations of Luneburg and Maxwell fish-eye lenses at the designed frequency f_0 = 40 kHz; (b) the Luneburg lens of 0.2 m diameter consisting of 373 hexagonal cells; (c) the excitation signal of a Gaussian pulse with the central frequency 40kHz; (d) the FFT of excitation signal.

In order to validate the wave focusing capability of the Luneburg and Maxwell fish-eye lenses designed above, the interaction of SH0 waves generated at finite sources with the lens is analyzed by finite element simulations. A transient SH0 wave signal is excited by a Gaussian pulse of the prescribed displacement in the y direction with the central frequency f_0 = 40 kHz. The excited signal is depicted in Fig. 2(c), as well as its FFT result shown in Fig. 2(d). In the x-y coordinate system with the origin located at the center of the lens, a uniform displacement excitation across the plate thickness is imposed at x = –0.2 m and –0.1 m < y < 0.1 m to generate a nearly plane SH0 wave for the Luneburg lens, as shown in Fig. 3(a). For the Maxwell fish-eye lens, a uniform line source across the plate thickness is assumed to excite a diverging wave at (–0.1 m, 0), which is located at the lens border, as shown in Fig. 4(a). The amplitudes of these excitation displacements are set arbitrarily due to the linearity of the problem. The region of the host plate to be discretized by finite elements is chosen separately for each lens accounting for the nature of incident wave field, i.e., –0.36 m < x < 0.44 m, –0.35 m < y < 0.35 m for the Luneburg lens and –0.2 m < x < 0.35 m and –0.25 m < y < 0.25 m for the Maxwell fish-eye lens. The low reflection boundary conditions available in Comsol Multiphysics are used at the outer boundaries of the discretized region in order to

eliminate unnecessary wave reflections. In the *x*-*y* plane, the maximum element size in the lens region is set as 3.6 mm, and gradually increased to 6 mm near the plate edges. On the other hand, the plate thickness (5 mm) is covered by one element considering the almost uniform distribution of u_y in the thickness direction. The implicit backward differentiation formula (BDF) is adopted for time integration with the time step fixed as 2×10^{-8} s. The simulated wave fields in the neighborhood of the lens are shown in Figs. 3 and 4. It can be seen in Figs. 3 and 4 that the SH0 wave travels faster close to the lens border than at the center, which makes the wavefront bend towards to the center. For both the Luneburg and Maxwell fish-eye lenses, the SH0 wave appears to focus on the opposite border as expected, i.e., (0.1 m, 0), and spreads out after passing through the lens, which validates the proposed design scheme. It should be pointed out that the excitation at the finite sources generates, besides SH0 waves, the S0-mode Lamb wave which travels in the *y*-direction in Figs. 3 and 4. In Fig. 3, the S0 wave does not interact with the Luneburg lens because it is generated on the outside of the lens and propagates in the *y* direction. In Fig. 4, the snapshots of contour curves have elliptic shapes due to the higher velocity of S0 wave than that of SH0 wave. The interaction region of the S0 wave and the Maxwell fish-eye lens is relatively small and it has negligible effect on the SH0 wave focusing.

Since the EFCs of the SH0 wave in the stubbed plate are nearly circular as shown in Section 2, it is expected that the two types of the lens designed above work for arbitrary direction of the incident wave. In order to confirm the omni-directional focusing performance, the excitation sources are rotated by 30° angle anticlockwise, as shown in Figs. 5 and 6. The wave focusing phenomena similar to Figs. 3 and 4 can be observed both for the Luneburg and Maxwell fish-eye lenses.

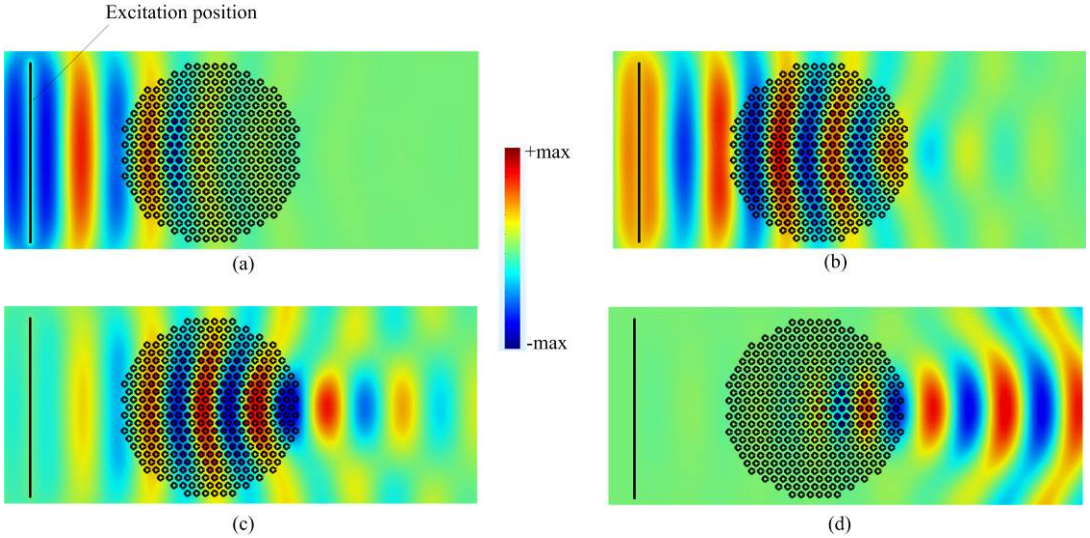

Figure 3 Instantaneous displacement fields of u_y (top view) for a plane SH0 wave excitation with 0° of incidence at different response times: (a) t = 0.2 ms; (b) t = 0.26 ms; (c) t = 0.3 ms; (d) t = 0.4 ms.

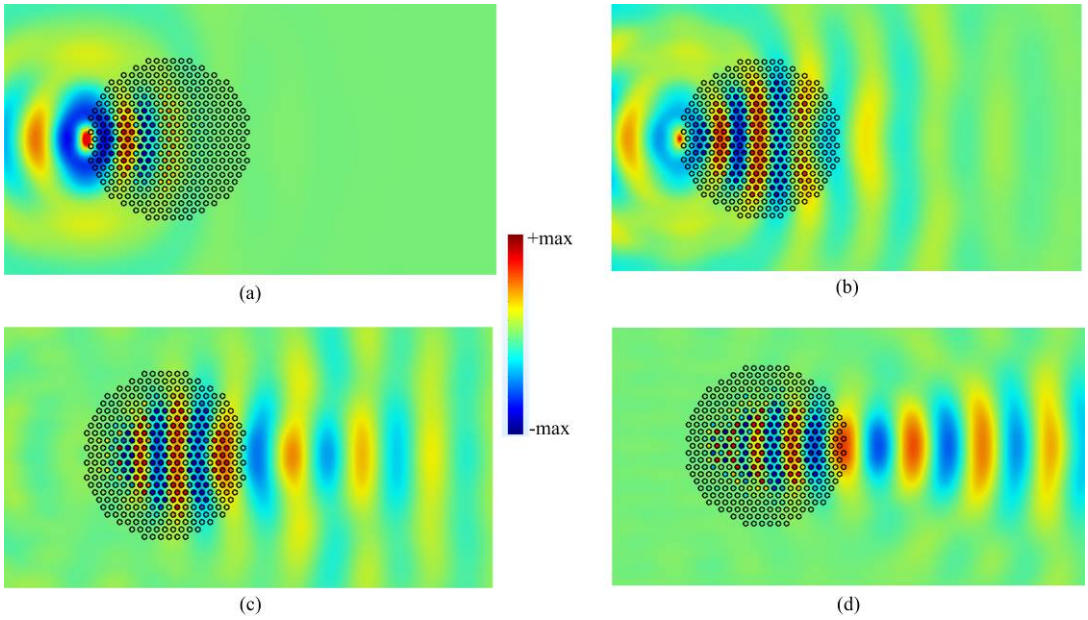

Figure 4 Instantaneous displacement fields of u_y (top view) for a point source SH0 wave excitation located at (–0.1 m, 0) for different response times: (a) t = 0.18 ms; (b) t = 0.28 ms; (c) t = 0.34 ms; (d) t = 0.4 ms.

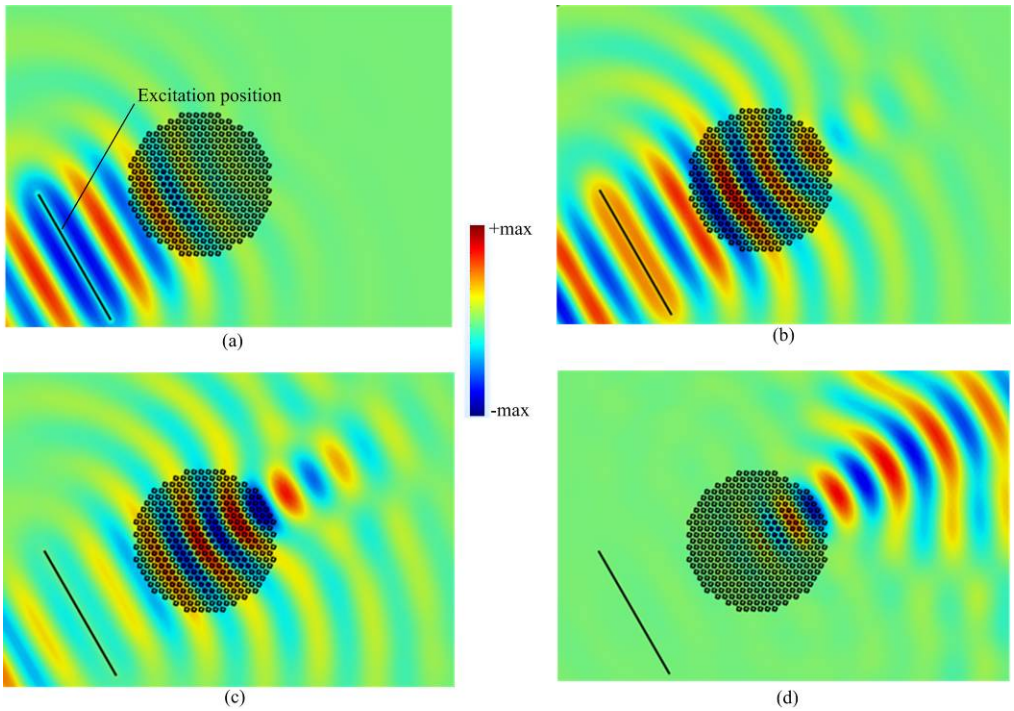

Figure 5 Instantaneous displacement fields (top view) for a plane SH0 wave excitation with 30° angle of incidence at different response times: (a) t = 0.2 ms; (b) t = 0.26 ms; (c) t = 0.3 ms; (d) t = 0.4 ms.

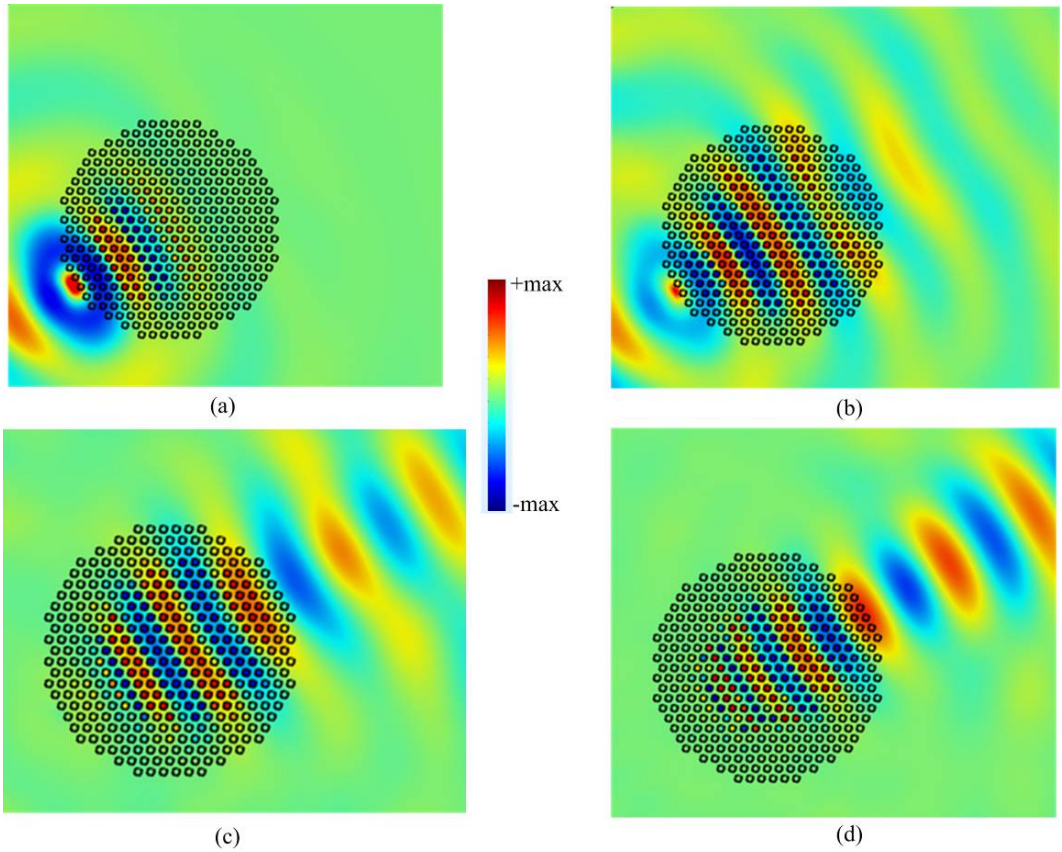

Figure 6 Instantaneous displacement fields (top view) for a point source SH0 wave excitation located at ($-0.05\sqrt{3}$ m, –0.05 m): (a) t = 0.18 ms; (b) t = 0.28 ms; (c) t = 0.34 ms; (d) t = 0.4ms.

Besides the time-domain analysis, the frequency-domain simulations are also carried out to quantitatively depict the wave focusing phenomena for the Luneburg and Maxwell fish-eye lenses. The models calculated in the frequency domain are the same as those in the time-domain analysis except that the excitation was made by the prescribed time-harmonic displacements with the frequency 40 kHz and that the discretized region of the plate, –0.28 m < x < 0.44 m and –0.165 m < y < 0.165 m for the Luneburg lens and –0.2 m < x < 0.36 m and –0.14 m < y < 0.14 m for the Maxwell fish-eye lens, is connected to perfectly matched layers (PMLs) at the outer boundaries to prevent the wave reflections instead of applying the low reflection boundary conditions. For the Luneburg lens, Fig. 7(a) shows the spatial distribution of $|u_y|^2$ as a measure of the local wave amplitude. For comparison, a flat plate without stubs is also simulated, with the result shown in Fig. 7(b). As shown in Fig. 7(c), the squared displacement amplitude at the point (0.1 m, 0) has been increased about 3 times of that at the same position without lens, which clearly shows the wave focusing phenomenon [35, 37]. Theoretically, the amplitude attains its maximum at (0.1 m, 0). Actually, the numerical result has the maximum amplitude at (0.0936 m, 0), which is nearly the same as the theoretical prediction. In this paper, a series of discrete stubs have been utilized to approximate the refraction index variation, which can be one of the reasons for the small discrepancy. The size of the focusing spot along the y direction at x = 0.1 m is evaluated by the 3-dB attenuation

level [40] of the displacement amplitude $|u_y|$, where $|u_y|^2$ reduces to a quarter of its peak as shown in Fig. 7(d). The focusing size in the y direction is evaluated as 0.856λ, where λ is the wavelength of the SH0 wave in the homogeneous plate at 40 kHz, which shows that a reasonable focusing is achieved.

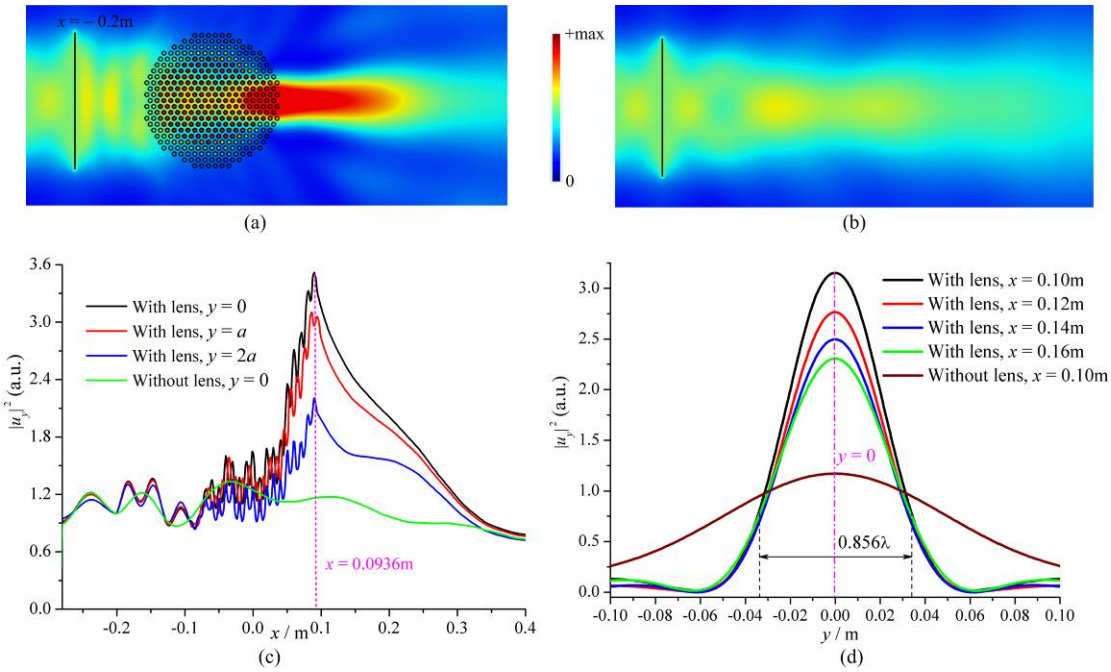

Figure 7 The spatial field distribution calculated in the frequency domain: (a) $|u_y|^2$ of the Luneburg lens (top view); (b) $|u_y|^2$ of an homogeneous plate without lens (top view); (c) $|u_y|^2$ profile in the x direction; (d) $|u_y|^2$ profile in the y direction. The profiles of (c) and (d) are at $z = h$ (the upper surface plane of the host plate).

As for the Maxwell fish-eye lens, the similar focusing phenomenon can be observed in Fig. 8. The focusing position is found to be at (0.09 m, 0), which has only small discrepancy from the theoretical prediction (0.1 m, 0). Since the SH0 wave generated at the point (–0.1 m, 0) spreads out rapidly, $|u_y|^2$ decreases quickly, which makes the amplitude at the focusing point smaller than that at the generation position, which was also found in Ref. [39]. However, $|u_y|^2$ at the focusing position is approximately five times larger than that at the corresponding point without the lens. Furthermore, the focusing size in the y direction is 0.931λ, which is also smaller than the wavelength in the homogeneous plate.

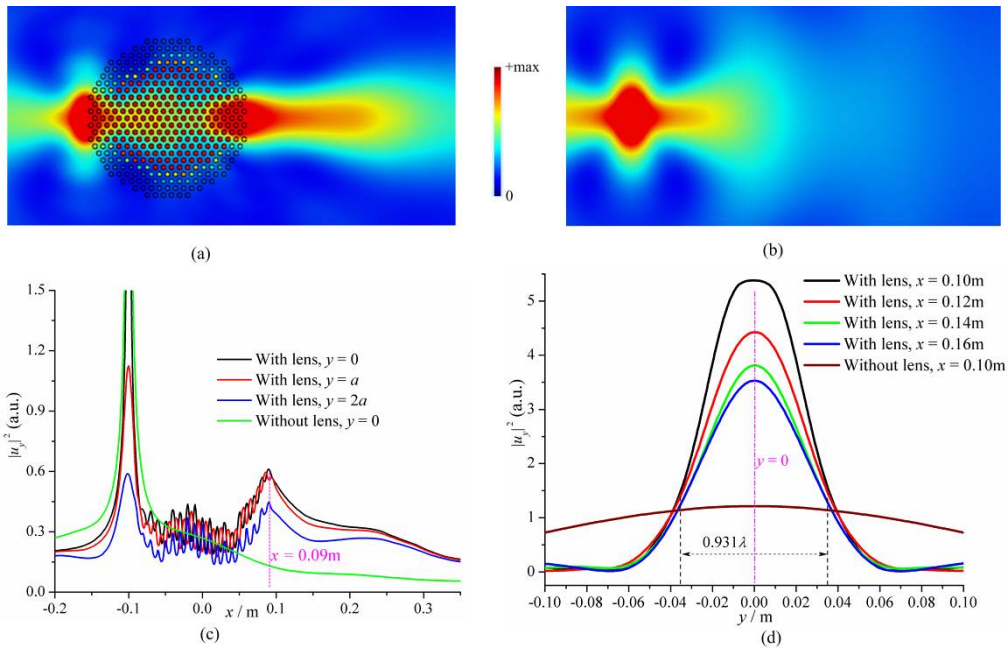

Figure 8 The spatial field distribution calculated in the frequency domain: (a) $|u_y|^2$ of the Maxwell fish-eye lens (top view); (b) $|u_y|^2$ of an homogeneous plate without lens (top view); (c) $|u_y|^2$ profile in the x direction; (d) $|u_y|^2$ profile in the y direction. The profiles of (c) and (d) are at $z = h$ (the upper surface plane of the host plate).

It has been revealed above that both the Luneburg and the Maxwell fish-eye lenses exhibit the expected wave focusing phenomenon at the designed frequency f = 40 kHz. Theoretically, this feature is only attained for the fixed frequency. However, the dispersion curves for different stub heights in Fig. 1(c) are nearly linear when the frequency is 40 kHz, which means that the phase velocity of SH0 wave will vary only by a small amount if the frequency changes nearby. Namely, it is anticipated that the two lenses designed in this paper can work effectively in a finite frequency range. When the frequency of the incident SH0 wave varies, the focusing location and the magnification ratio will vary. In order to quantitatively demonstrate the applicability of the two lenses at other frequencies, the same simulations as those shown above were performed for different frequencies near 40 kHz. In order to evaluate if the focusing is achieved or not, we define the following criteria: (1) the (0.1 m, 0) point should be located in the region of half bandwidth defined by the 3-dB attenuation of the displacement amplitude; (2) the distance between the focusing point and (0.1 m, 0) should be smaller than the half of the wavelength in the substrate plate at the frequency at hand. The focusing for the assumed frequency was judged to be valid when both of these conditions are satisfied simultaneously.

With the help of the criteria defined above, the effective frequency range can be obtained as 32.5 kHz to 46.4 kHz for the Luneburg lens, and correspondingly as 36.6 kHz to 41.3 kHz for the Maxwell fish-eye lens. Some representative cases are shown in Figs. 9 and 10. The narrower bandwidth of the Maxwell fish-eye lens can be interpreted as follows. The stub at the center of the Maxwell fish-eye lens is higher than that of the Luneburg lens. The frequency dispersion curve near 40 kHz in Fig. 1(c) exhibits stronger non-linearity for a

higher stub, which gives a smaller effective frequency range for the Maxwell fish-eye lens. Additionally, for a higher frequency, the slowing effect of the stubs near the center is more evident, which drags the SH0 wave more significantly and makes the SH0 wave front bend towards the center earlier. Therefore, with the increasing frequency, the focusing location of the two lenses gradually moves towards the interior of the lens as can be seen in Figs. 9 and 10.

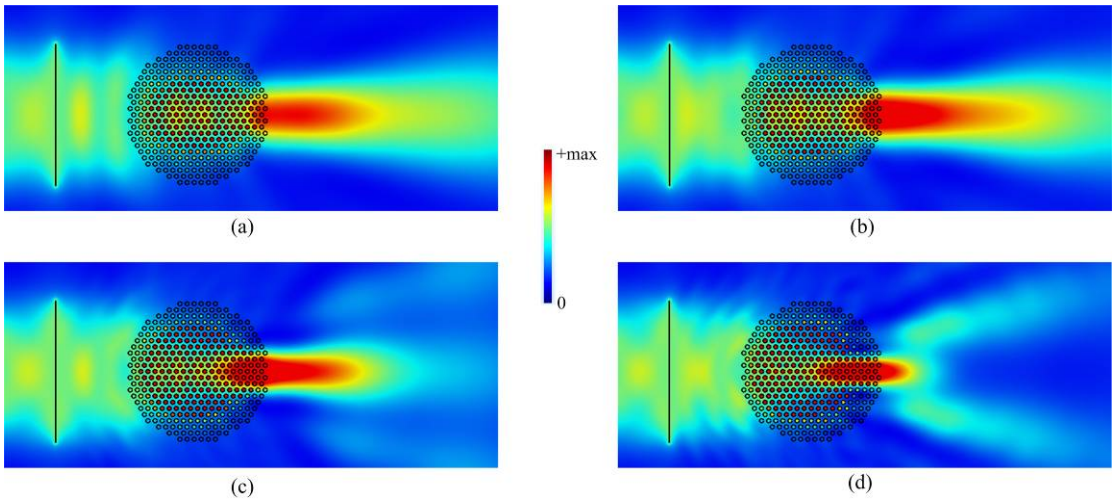

Figure 9 The displacement amplitude distributions (top view) of the Luneburg lens for different excitation frequencies: (a) f = 33 kHz; (b) f = 36 kHz; (c) f = 42 kHz; (d) f = 46 kHz.

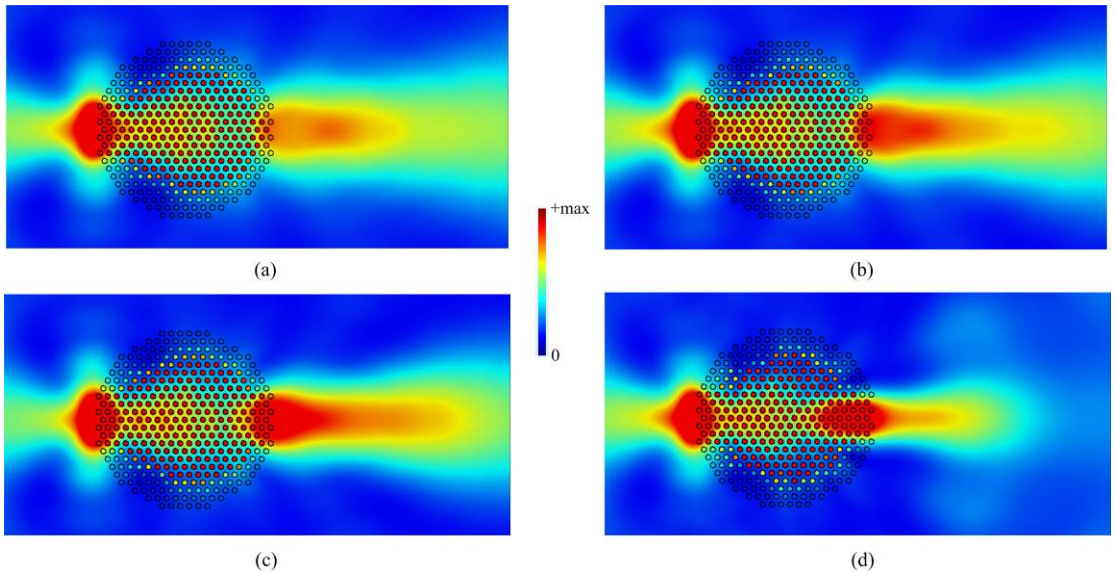

Figure 10 The displacement amplitude distributions (top view) of the Maxwell fish-eye lens for different excitation frequencies: (a) f = 37 kHz; (b) f = 38 kHz; (c) f = 39 kHz; (d) f = 41 kHz.

Until now, the anomalous focusing phenomenon of SH0 waves has been fulfilled successfully with the aid of the Luneburg and Maxwell Fish-Eye lenses, which consists of graded stubs hexagonally distributed on one surface of an aluminum plate. Accompanying

SH0 wave propagation, mode conversion, caused by the asymmetrical structure, takes place in the lenses (see Appendix for a detailed comparison). However, totally speaking, the shear horizontal displacement is dominated in the working frequency designed, and the mode conversion has negligible effect on the wave focusing phenomenon. It should also be stressed here that the design methodology proposed here is widespread, which is suitable for the other lens, *e.g.*, gradient-index lens [41-42], as long as the working frequency is beyond of band gaps.

4 *An SH0 wave-based low-pass wave filter*

In this section, an aluminum plate with graded multiple stubs is designed, through which the SH0 wave can be manipulated by the frequency filtering property. Metamaterial-based frequency separation filters have been considered in Ref. [31, 43-45], in particular, by Li and Cheng [31] for SH0 waves using graded stub heights in one direction. In this section, the idea studied in Ref. [31] is extended to realize an SH wave-based frequency filter for a localized wave source in plates. Before the structural design, the evolution of the first complete BG of the periodic stubbed plate with respect to the stub height h' is calculated and depicted in Fig. 11. Here, the complete BG is obtained by the analysis based on the model in Section 2 but for all wave vectors along the boundary of the first Brillouin zone. It can be seen that the first complete BG is shifted gradually and its bottom edge frequency decreases continuously from 168 kHz to 30 kHz when h' increases, pointing at the possibility of tuning BGs through changing the stub height. If the stub height is graded spatially, incident SH0 waves with different frequencies will be reflected at different positions. Furthermore, the group velocity of SH0 waves decreases in different levels for different frequencies, as expected from the dispersion curves in Fig. 1(c) which become relatively flat near the M point.

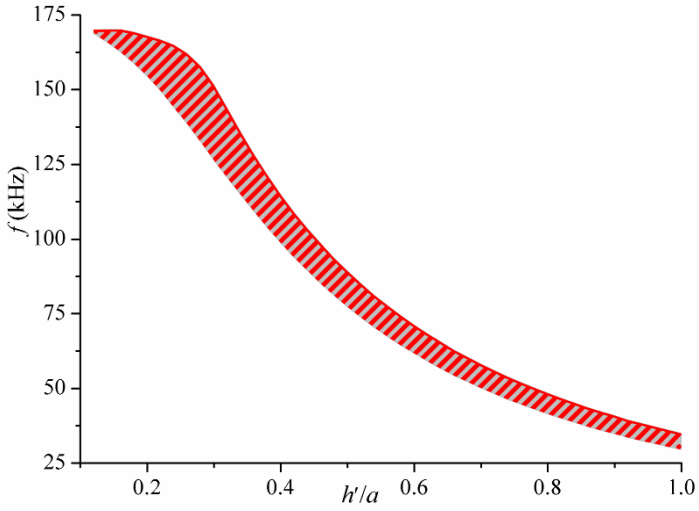

Figure 11 Evolution of the first BG of SH0 wave with respect to stub height h'.

Based on the idea described above, an SH0 wave-based low-pass wave filter with graded stubs is proposed, with its shape shown in Fig. 12. Our aim is to separate SH0 wave signals

with different frequencies through the BG and the velocity reduction phenomenon. There are multiple stubs, analyzed in Section 2, hexagonally distributed on the surface of an aluminum plate, with the stub height h' changing linearly in the form of $h'(r) = a(r - r_1)/(R_1 - r_1)$, where r_1 = 0.1 m and R_1 = 0.42 m. At the origin of the coordinated system, the SH0 wave is assumed to be generated by a uniform displacement excitation in the y direction across the plate thickness. The filter occupies the intersection of 0.1 m ≤ x ≤ 0.42 m and 0.1 m ≤ r ≤ 0.42 m, where r stands for the distance from the origin. Comprehensive FEM simulations, in both time and frequency domains, are carried out to show the frequency separation capability of the low pass wave filter.

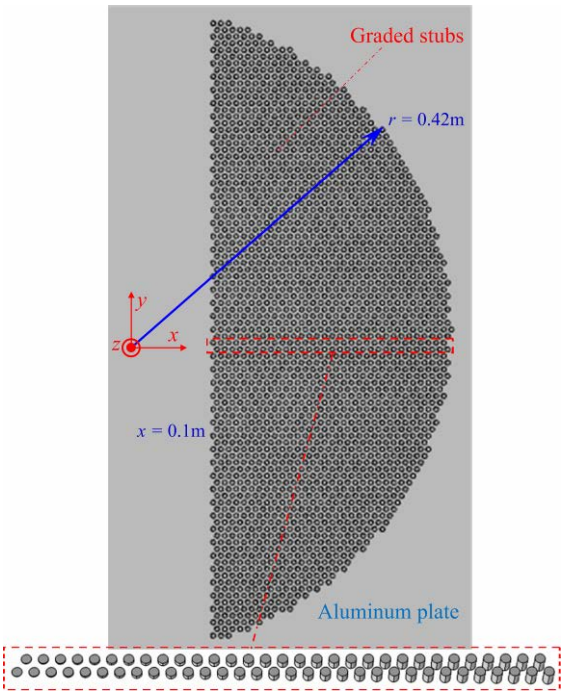

Figure 12 Schematic of the SH0 wave-based low-pass wave filter with graded stubs. The stubs are arranged on the intersection of 0.1 m ≤ x ≤ 0.42 m and 0.1 m ≤ r ≤ 0.42 m with the height h' changing linearly from zero to a.

For the time domain analysis, a Gaussian displacement pulse u_y with its central frequency f_0 = 50 kHz is imposed at the origin across the plate thickness, which simultaneously generates both S0 wave and SH0 wave. The surrounding host plate is discretized for the region –0.05 m < x < 0.49 m and –0.45 m < y < 0.45 m. Similar to the analysis for the Luneburg lens and Maxwell fish-eye lens, the outer boundaries of the plate are set as low reflection boundaries. The maximum element size in the stub region is 4.8 mm, and gradually increased to 8 mm near the plate edges. The implicit solver and the time step are the same as the analysis for the Luneburg lens and Maxwell fish-eye lens. The screenshots at some specific time points, depicted in Fig. 13, clearly show the wave propagation process. Because of the difference in the velocities of S0 and SH0 waves, the wavefront near the origin has an elliptic shape as shown in Fig. 13(a). Since the generation position is at a certain

distance away from the wave filter, the S0 wave will propagate freely in the y direction. Therefore, the unavoidable S0 components will have negligible effect on the SH0 wave interaction with the stub arrangement. With the increasing stub height along the r direction, the wave-slowing effect becomes more and more evident. The generated SH0 wave signal appears to be compressed gradually with its wavelength becoming shorter and shorter, as shown in Fig. 13(b). Reviewing Fig. 11, we can conclude that the SH0 wave can propagate in the plate if the stub height is smaller than 0.72 a. Owing to the wave prohibition effect caused by band gaps, theoretically, the furthest distance the SH0 wave can reach is r = 0.33 m. In the numerical result, it arrives at about r = 0.36 m, as shown in Fig. 13(c). The small discrepancy originates from the wideband property of the incident signal. After complex interaction (Brag scattering effect) caused by graded stubs, the SH0 wave will be reflected, as shown in Fig. 13(d) when t = 0.52 ms.

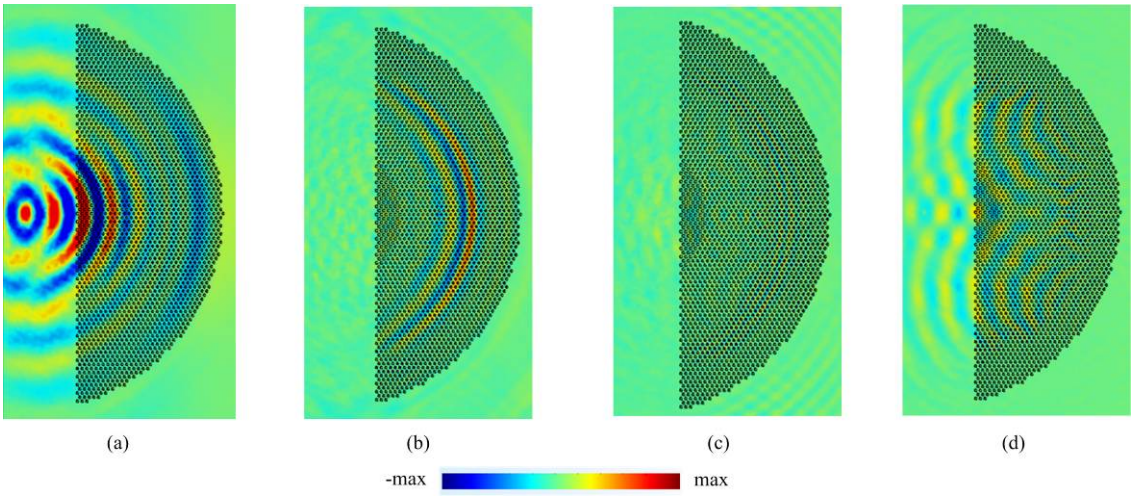

Figure 13. Displacement profiles (top view) of the SH0 waves at some specific time instants: (a) t = 0.15 ms; (b) t = 0.24 ms; (c) t = 0.32 ms; (d) t = 0.52 ms.

Following the analysis in the time domain, a series of simulations are performed in the frequency domain. The plate is discretized for the region –0.06 m < x < 0.5 m and –0.43 m < y < 0.43 m and is connected to PMLs at the outer boundaries. For different frequencies in the range from 20 kHz to 80 kHz, the wave is excited by the displacement u_y of unit amplitude at the same location as in the frequency-domain analysis. The simulations yield the distributions of $|u_y|$ for some frequencies shown in Fig. 14. It clearly shows the frequency separation, i.e., the SH0 wave with a lower frequency can travel over a longer distance from the excitation point. The wave amplitude is concentrated in the form of a circle, not in a line as in Ref. [31], due to the different excitation condition and the wave diffraction effect. Taking f = 80 kHz for example, the energy is mainly concentrated in the region of $r \le 0.26\text{m}$, as shown in Fig. 14(a). The stub height at r = 0.26 m is h' = 0.5a, which is consistent with the critical stub height corresponding to the BG in Fig. 11.

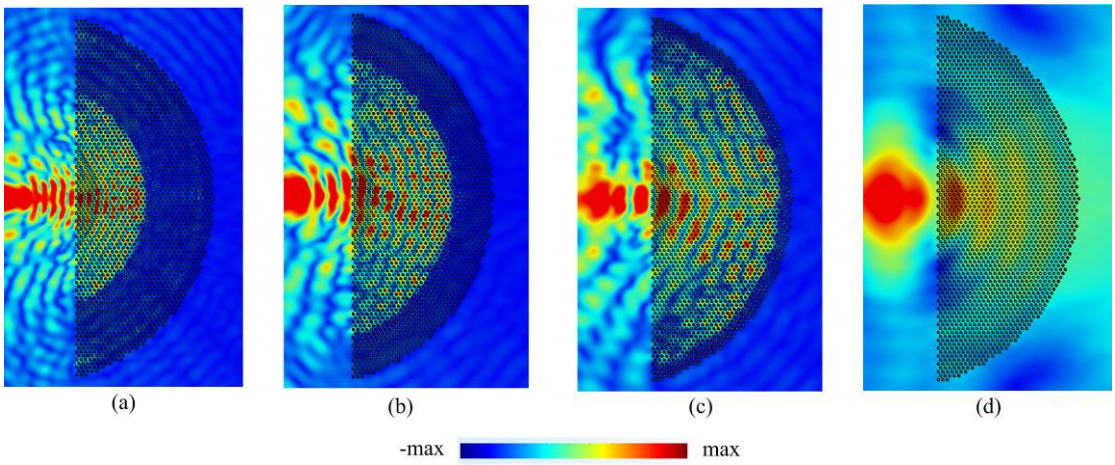

Figure 14 Displacement amplitude distributions (top view) for different frequencies: (a) 80 kHz; (b) 50 kHz; (c) 35 kHz; (d) 20 kHz.

In order to quantify the frequency separation effect, the wave is observed at four different locations, i.e., (0.15 m, 0), (0.25 m, 0), (0.35 m, 0) and (0.45 m, 0), and the corresponding displacement amplitude are displayed in Fig. 15. The stub height at x = 0.15 m is 0.1a, and hence the SH0 wave with the frequency ranging from 20 kHz to 100 kHz can be transmitted as shown in Fig. 15. However, at x = 0.35 m, corresponding to the stub height 0.78a, the waves with the frequency larger than about 42 kHz have not been transmitted through the wave filter, which can be expected from Fig. 11. The bottom edge of the first BG in Fig. 11 changes continuously and monotonously, which means that the linearly distributed stubs higher than 0.78a are simultaneously taking effect to block the SH0 wave propagation. If the receiving position is located beyond the wave filter, such as x = 0.45 m in Fig. 15, the wave with the frequency below 30 kHz can only be observed. Therefore, the plate with graded stubs in Fig. 12 can be viewed as a low-pass wave filter. The SH0 wave with a lower frequency travels over longer distance while the waves with higher frequencies stop and are reflected at certain locations. This type of stub structure may be useful to pick up the wave with a specific frequency at a certain distance from the excitation point if it is combined with an arch-shaped transducer.

In Fig. 15, we can also observe that high peak values of $|u_y|$ appear just before the attenuation region, which is in agreement with the work by Li and Cheng [31]. This can be explained by the reduction of the velocity of SH0 wave during the propagation process, which makes its wavelength shorter and leads to larger displacement amplitudes before the attenuation.

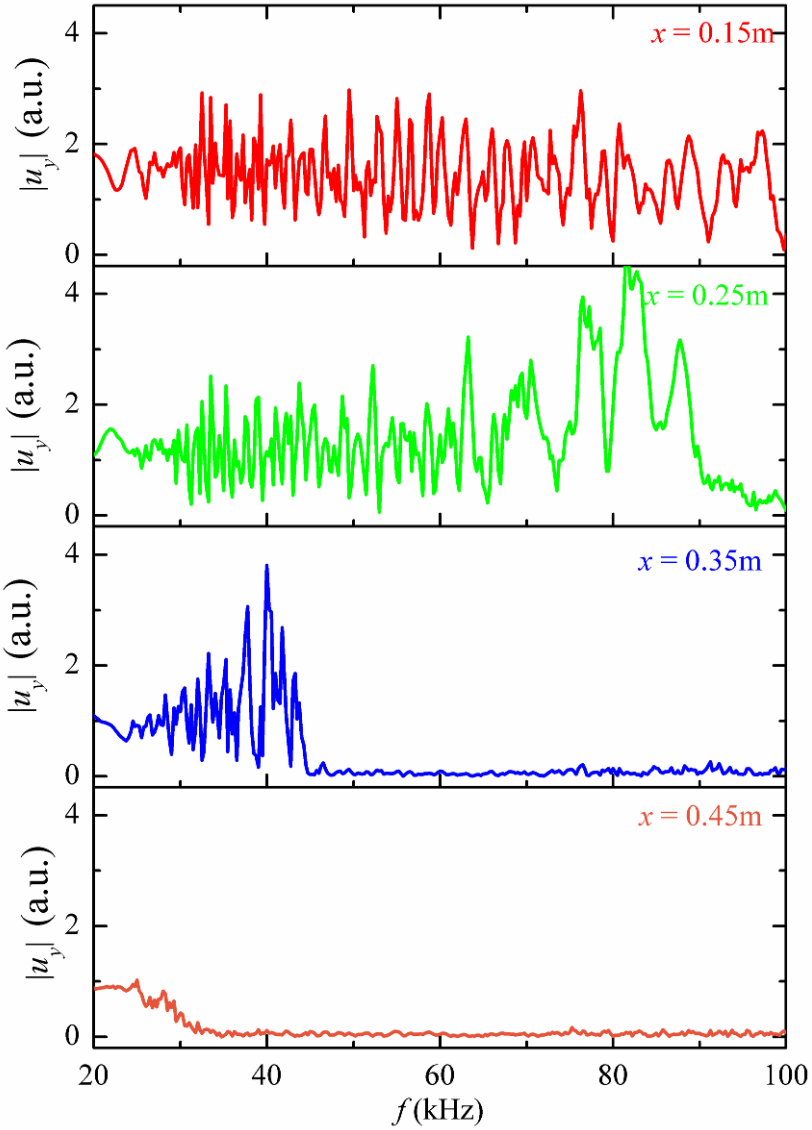

Figure 15 Displacement amplitude response at different positions.

5 *Conclusions*

In this paper, based on the band structure analysis of SH0 waves in an aluminum plate with cylindrical stubs hexagonally distributed on the surface, SH0 wave-based Luneburg and Maxwell fish-eye lenses, as well as low-pass wave filter, have been designed by spatially grading the height of stubs. The present study reveals the following conclusions:

1) A plane SH0 wave (or an SH0 wave emitted from a point-source at the lens edge) can be focused on the opposite border when it travels through the Luneburg lens (or the Maxwell fish-eye lens). The lenses exhibit good omni-directional and focusing capability, with the focusing size smaller than the wavelength. Additionally, both of the designed lenses can work in a finite frequency range, and the effective frequency range of the Luneburg lens is larger than that of the Maxwell fish-eye lens.

2) The first complete BG of the SH0 wave changes monotonically with the stub height.

Inspired by this relation, an SH0 wave based low-pass wave filter is designed with the linear spatial distribution of the stub height. The SH0 wave with a lower frequency can travel over a longer distance through this filter. Therefore, the wave filter can be applied for frequency separation.

As a final remark, the design scheme in this paper is relatively simple and convenient for practical applications, which is expected to be fulfilled in the near future.

Acknowledgments

The authors gratefully acknowledge the supports of the Postdoctoral Fellowships for Research in Japan (FY2018 P18043) and the Grant-in-Aid for JSPS Fellows (18F18043) by the Japan Society for the Promotion of Science (JSPS), Natural Science Foundation of Shaanxi Province of China (2018JM1039), and Project Funded by China Postdoctoral Science Foundation (2018M640975).

References

[1] Mitra M and Gopalakrishnan S 2016 Guided wave based structural health monitoring: A review *Smart Materials and Structures* **25** 053001
[2] Giurgiutiu V 2014 *Structural Health Monitoring with Piezoelectric Wafer Active Sensors* (Elsevier)
[3] Belanger P and Boivin G 2016 Development of a low frequency omnidirectional piezoelectric shear horizontal wave transducer *Smart Mater. Struct.* **25** 045024
[4] Li P, Shan S B, Wen F Z and Cheng L 2019 A fully-coupled dynamic model for the fundamental shear horizontal wave generation in a PZT activated SHM system *Mech. Syst. Signal Process.* **116** 916–32
[5] Lissenden C, Liu Y, Choi G W and Yao X 2014 Effect of localized microstructure evolution on higher harmonic generation of guided waves *J. Nondestructive Eval.* **33** 178–86
[6] Rocha-Gaso M-I, March-Iborra C, Montoya-Baides Á and Arnau-Vives A 2009 Surface generated acoustic wave biosensors for the detection of pathogens: A review *Sensors* **9** 5740–69
[7] Wang W and He S T 2009 Theoretical analysis on response mechanism of polymer-coated chemical sensor based Love wave in viscoelastic media *Sensor. Actuat. B-Chem.* **138** 432–440
[8] Wu H Y, Xiong X M, Zu H F, Wang J H-C and Wang Q M 2017 Theoretical analysis of a Love wave biosensor in liquid with a viscoelastic wave guiding layer *J. Appl. Phys.* **121** 054501
[9] Zaitsev B D, Kuznetsova I E, Joshi S G and Borodina I A 2001 Acoustic waves in piezoelectric plates bordered with viscous and conductive liquid *Ultrasonics* **39** 45–50
[10] Chen X and Liu D L 2010 Analysis of viscosity sensitivity for liquid property detection applications based on SAW sensors *Mat. Sci. Eng. C-Mater.* **30** 1175–82
[11] Goto M, Yatsuda H and Kondoh J 2013 Analysis of mass loading effect on guided shear horizontal surface acoustic wave on liquid/Au/quartz structure for biosensor application *Jpn. J. Appl. Phys.* **52** 07HD10

[12] Zhou W, Li H and Yuan F G 2014 Guided wave generation, sensing and damage detection using in-plane shear piezoelectric wafers *Smart Mater. Struct.* **23** 015014
[13] Miao H C, Huan Q and Li F X 2016 Excitation and reception of pure shear horizontal waves by using face-shear d_{24} mode piezoelectric wafers *Smart Mater. Struct.* **25** 11LT01
[14] Boivin G, Viens M and Belanger P 2018 Plane wave SH0 piezoceramic transduction optimized using geometrical parameters *Sensors* **18** 542
[15] Miao H C, Huan Q, Li F X and Kang G Z 2018 A variable-frequency bidirectional shear horizontal (SH) wave transducer based on dual face-shear (d_{24}) piezoelectric wafers *Ultrasonics* **89** 13–21
[16] Khelif A, Choujaa A, Djafari-Rouhani B, Wilm M, Ballandras S and Laude V 2003 Trapping and guiding of acoustic waves by defect modes in a full-band-gap ultrasonic crystal *Phys. Rev. B* **68** 214301
[17] Zhang X D and Liu Z Y 2004 Negative refraction of acoustic waves in two-dimensional phononic crystals *Appl. Phys. Lett.* **85** 341–3
[18] Bucay J, Roussel E, Vasseur J O, Deymier P A, Hladky-Hennion A C, Pennec Y, Muralidharan K, Djafari-Rouhani B and Dubus B 2009 Positive, negative, zero refraction, and beam splitting in a solid/air phononic crystal: Theoretical and experimental study *Phys. Rev. B* **79** 214305
[19] Wen J H, Yu D L, Cai L and Wen X S 2009 Acoustic directional radiation operating at the pass band frequency in two-dimensional phononic crystals *J. Phys. D Appl. Phys.* **22** 115417
[20] Liang Z X and Li J S 2012 Extreme acoustic metamaterial by coiling up space *Phys. Rev. Lett.* **108** 114301
[21] Yuan B, Liang B, Tao J C, Zou X Y and Cheng J C 2012 Broadband directional acoustic waveguide with high efficiency *Appl. Phys. Lett.* **101** 043503
[22] Zigoneanu L, Popa B I and Cummer S A 2014 Three-dimensional broadband omnidirectional acoustic ground cloak *Nat. Mater.* **13** 352–5
[23] Wang G, Jin L, Xu Z and Li P 2016 Acoustically induced transparency by using concentric spherical shells with coaxial aperture array *Appl. Phys. Lett.* **109** 073503
[24] Dubois M, Shi C Z, Zhu X F, Wang Y and Zhang X 2017 Observation of acoustic Dirac-like cone and double zero refractive index *Nat. Commun.* **8** 14871
[25] Kushwaha M S, Halevi P, Dobrzynski L and Djafari-Rouhani B 1993 Acoustic band structure of periodic elastic composites *Phys. Rev. Lett.* **71** 2022–5
[26] Biwa S, Yamamoto S, Kobayashi F and Ohno N 2004 Computational multiple scattering analysis for shear wave propagation in unidirectional composites *Int. J. Solids Struct.* **41** 435–57
[27] Kobayashi F, Biwa S and Ohno N 2004 Wave transmission characteristics in periodic media of finite length: multilayers and fiber arrays *Int. J. Solids Struct.* **41** 7361–75
[28] Barnwell E G, Parnell W J and Abrahams I D 2016 Antiplane elastic wave propagation in pre-stressed periodic structures: tuning, band gap switching and invariance *Wave Motion* **63** 98–110
[29] Norris A N and Parnell W J 2012 Hyperelastic cloaking theory: transformation elasticity with pre-stressed solids *P. Roy. Soc. A-Math. Phy.* **468** 2881–903
[30] Parnell William J and Shearer T 2013 Antiplane elastic wave cloaking using

metamaterials, homogenization and hyperelasticity *Wave Motion* **50** 1140–52
[31] Li P and Cheng L 2018 Shear horizontal wave propagation in a periodic stubbed plate and its application in rainbow trapping *Ultrasonics* **84** 244–53
[32] Cao L Y, Yang Z C and Xu Y L 2018 Steering elastic SH waves in an anomalous way by metasurface *J. Sound Vib.* **418** 1–14
[33] Liu W and Su X Y 2010 Collimation and enhancement of elastic transverse waves in two-dimensional solid phononic crystals *Phys. Lett. A* **374** 2968–71
[34] Climente A, Torrent D and Sanchez-Dehesa J 2014 Gradient index lenses for flexural waves based on thickness variations *Appl. Phys. Lett.* **105** 064101
[35] Yuan B G, Tian Y, Cheng Y and Liu X J 2016 An acoustic Maxwell's fish-eye lens based on gradient-index metamaterials *Chinese Phys. B* **25** 104301
[36] Tol S, Degertekin F L and Erturk A 2017 Phononic crystal Luneburg lens for omnidirectional elastic wave focusing and energy harvesting *Appl. Phys. Lett.* **111** 013503
[37] Jin Y B, Torrent D, Pennec Y, Pan Y D and Djafari-Rouhani B 2016 Gradient index devices for the full control of elastic waves in plates *Sci. Rep.* **6** 24437
[38] Kim S H 2014 Cylindrical acoustic Luneburg lens 2014 *8th International Congress on Advanced Electromagnetic Materials in Microwaves and Optics*, **pp** 364–6
[39] Torrent D, Pennec Y and Djafari-Rouhani B 2014 Omnidirectional refractive devices for flexural waves based on graded phononic crystals *J. Appl. Phys.* **116** 224902
[40] Qi S B, Li Y and Assouar B 2017 Acoustic focusing and energy confinement based on multilateral metasurfaces *Phys. Rev. Appl.* **7** 054006
[41] Darabi A, and Leamy M J 2018 Analysis and experimental validation of an optimized gradient-index phononic-crystal lens *Phys. Rev. Appl.* **10** 024045
[42] Zareei A, Darabi A, Leamy M J, and Alam M-R 2018 Continuous profile fexural GRIN lens: Focusing and harvesting flexural waves *Appl. Phys. Lett.* **112** 023901
[43] Zhao D G, Li Y and Zhu X F 2015 Broadband Lamb wave trapping in cellular metamaterial plates with multiple local resonances *Sci. Rep.* **5** 9376
[44] Xu Y L and Peng P 2015 High quality broadband spatial reflections of slow Rayleigh surface acoustic waves modulated by a graded grooved surface *J. Appl. Phys.* **117** 035103
[45] Xu Y L 2015 Spatial bandwidth enlargement and field enhancement of shear horizontal waves in finite graded piezoelectric layered media *Phys. Lett. A* **379** 1752–6

Appendix: Mode conversion in the lenses

In order to clearly demonstrate the mode conversion when SH0 wave propagates, Figs. 16 shows the distributions of $|u_x|^2$, $|u_y|^2$ and $|u_z|^2$ at f = 40kHz in the Luneburg lens, from which we can see the mode conversion in the lens, i.e., Lamb waves have been excited by the incident SH0 waves. So it is in the Maxwell fish-eye lens shown in Fig. 17. Mode conversion in the Maxwell fish-eye lens is more evident than that in the Luneburg lens. However, compared with $|u_x|^2$ and $|u_z|^2$, $|u_y|^2$ is dominated, which means that the shear displacement is the main component, and the mode conversion has negligible effect on the wave focusing phenomenon.

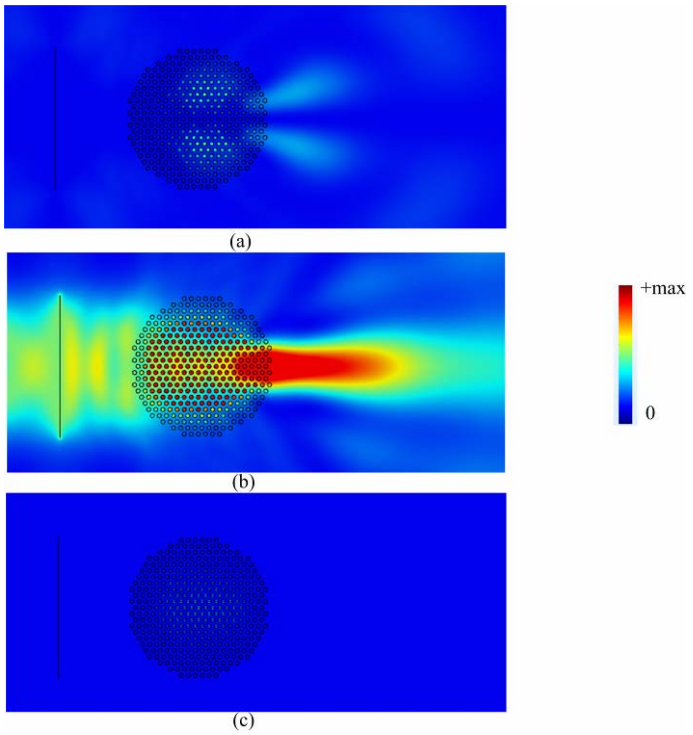

Figure 16 The spatial field distributions (top view) of the Luneburg lens at f = 40 kHz: (a) $|u_x|^2$; (b) $|u_y|^2$; (c) $|u_z|^2$.

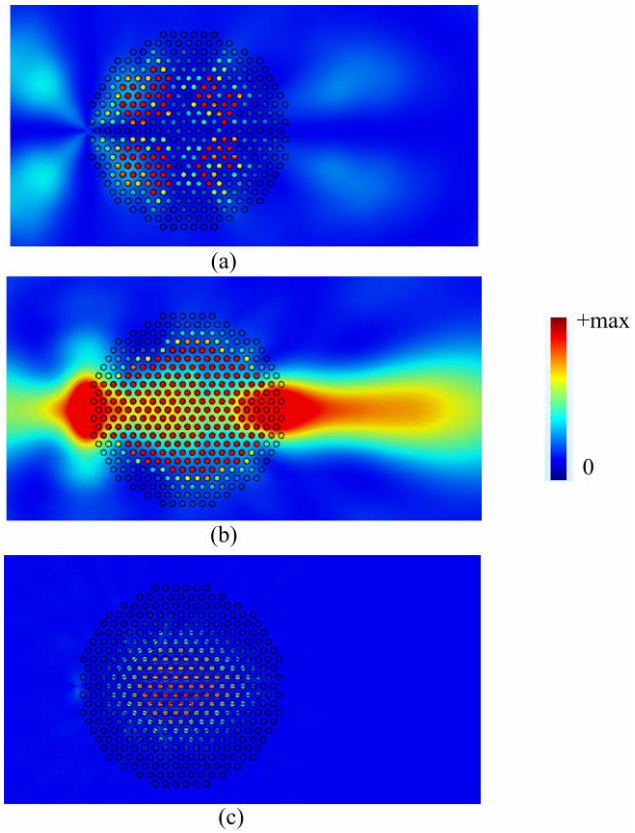

Figure 17 The spatial field distributions (top view) of the Maxwell fish-eye lens at f = 40 kHz: (a) $|u_x|^2$; (b) $|u_y|^2$; (c) $|u_z|^2$.